Accurate 3D stopping-power ratio estimation by statistical image reconstruction from dual energy CT sinogram data exported from a commercial multi-slice CT scanner

Washington University in St. Louis
James McKelvey School of Engineering

Maria Medrano, Tao Ge, David G. Politte, Jeffrey F. Williamson, Tianyu Zhao, Ruirui Liu, Rui Liao, Mariela A. Porras-Chaverri, Bruce R. Whiting, Joseph A. O'Sullivan.

University of Pittsburgh
Universidad de Costa Rica

1. MOTIVATION

- **Proton radiotherapy (PT)** Offers comparable effectiveness to **photon radiotherapy** but with less toxicity[1,2].
- **PT effectiveness** requires accurate knowledge of Bragg peak fall-off at the end of the proton-beam range so SOBP falloff can be accurately aligned with the Clinical Target Volume (CTV) distal boundary.
- **Previously, we demonstrated that our 2D Joint Statistical Image Reconstruction code using a basis-vector cross-section model (JSIR-BVM)** more accurately maps stopping power ratios (SPR) and better suppresses noise than competing image- and sinogram-domain dual-energy CT (DECT)[3,4].
- **Goals: (1)** eliminate up to 2/3 of range uncertainty (currently 2-3.5%) in current clinical practice. **(2)** Make JSIR-BVM clinically feasible for PT planning.
- **Clinical feasibility requires that JSIR-BVM be extended to 3D image reconstruction from helical sinograms in a reasonable time.** To this end, we herein **(1)** present our **GPU-based 3D JSIR-BVM** reconstruction engine and **(2)** quantitatively assess its performance on simulated and experimentally acquired helical sinograms for phantom and patient scan subjects.

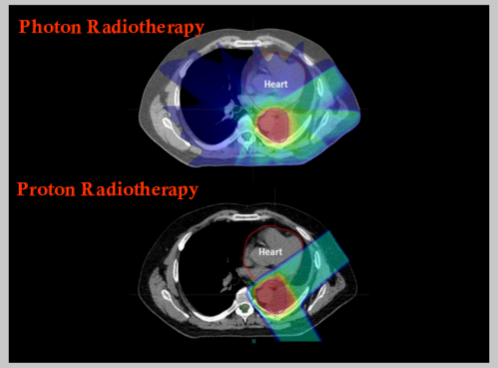

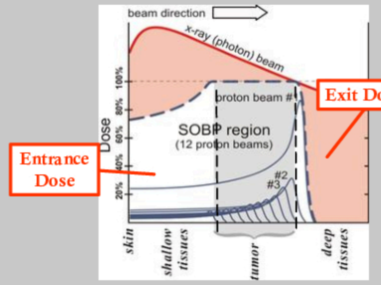

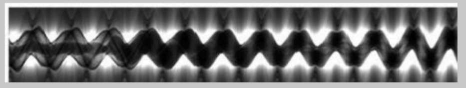

Measurement Space to Image Space

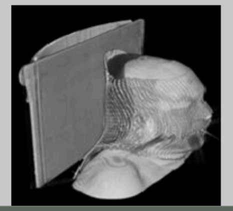

2. JSIR-BVM RECONSTRUCTION

- **3D JSIR-BVM:** Reconstruct 3D CT images of polystyrene and $CaCl_2$ solution basis-material weights. $c_1(x)$ and $c_2(x)$ from 90 kVp and 140 kVp sequentially acquired polyenergetic helical transmission sinograms, $d_j(y)$, by solving a penalized maximum likelihood estimation (MLE) problem[5,6].

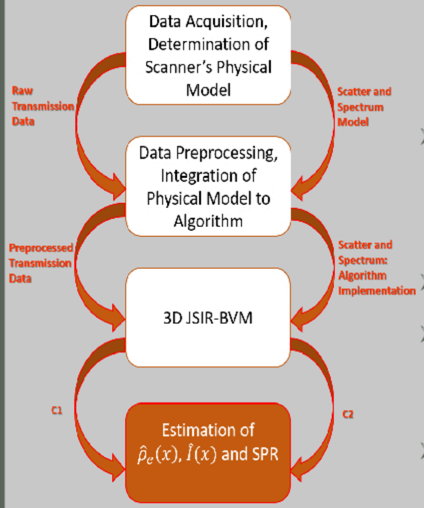

- Transmission sinograms are independently Poisson distributed random variables with means

$$Q_j\,(y{:}\mu) = I_{o,y}\,(y)\sum_E \psi_j(y,E)\,e^{-\sum_x h(y|x)\sum_{i=1}^{2} c_i(x)\mu_i(E)} + \gamma_j(y),$$

  where μ_i are the linear attenuation coefficients of each base material, $\psi_j(y,E)$ denotes the j-th photon spectrum, and $\gamma_j(y)$ the scattered-photon sinogram.
- Use MLE to find $(c_1(x), c_2(x))$ that minimizes the I-divergence between measured and predicted sinograms[7]

$$I_d(d_j\|Q_j) = \sum_y \left(d_j(y)\log\frac{d_j(y)}{Q_j(y)} - d_j(y) + Q_j(y)\right)$$

- Final Objective function[8]: $g(c_1,c_2) = \sum_{j=L,H} I_d\,(d_j\|Q_j) + \lambda\sum_{i=1}^{2} R(c_i)$
- BVM weights are used to derive pixel-wise estimates of electron density, $\hat{\rho}_e(x)$, and mean excitation energy, $\hat{I}(x)$ [5,6].
  - For example, **Electron Density** $= \hat{\rho}_e(x) = c_1(x)\rho_{e,1} + c_2(x)\rho_{e,2}(x)$
- Estimate stopping power using simplified **Bethe-Bloch Equation.**

$$\hat{S}_p(E_p,x) = -\frac{dE_p}{dx}(x) = \hat{\rho}_e\,(x)\frac{k_1}{\beta^2}\left[\frac{1}{2}\ln\frac{k_2\beta^2 T_{max}}{\hat{I}(x)^2(1-\beta^2)} - \beta^2\right]$$

3. GPU ARCHITECTURE

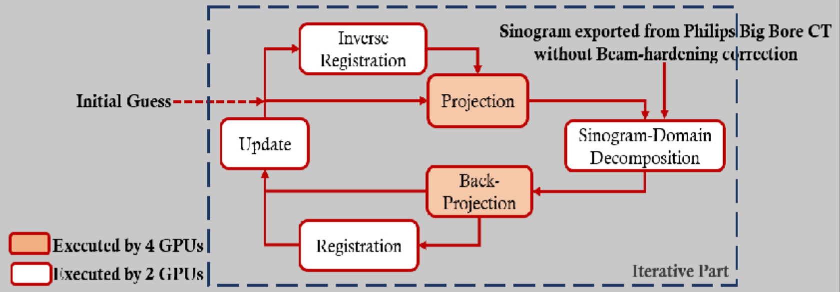

Our GPU code uses branchless distance-driven forward and back-proejectors. Projected values are weighted based on the intersection volume between rays and image voxels. Each iteration requires 4 forward- and 8 back-projections, accounting for ~90% of the total elapsed time. Deformable image registration is introduced to address possible organ motion between the sequentially acquired 90 and 140 kVp image sets.

Category	Material	Composition	Density (g/mL)	SPR
Soft	Water	H_2O	0.998	1.000
	Acetone	C_3H_6O	0.788	0.796
	Ethanol	C_2H_5OH	0.789	0.820
	n-Propanol	C_3H_7OH	0.803	0.841
	n-Butanol	C_4H_9OH	0.807	0.848
Bony	CaCl-1	$CaCl_2$(7.20%)	1.052	1.037
	CaCl-2	$CaCl_2$(18.24%)	1.153	1.110
	CaCl-3	$CaCl_2$(23.07%)	1.202	1.144
	KP-1	K_2HPO_4(9.37%)	1.075	1.058
	KP-2	K_3HPO_4(17.17%)	1.149	1.114
	KP-3	K_2HPO_4(29.26%)	1.273	1.206
	KP-4	K_2HPO_4(45.21%)	1.467	1.346

Known properties of simulated inserts.

Category	Material	Composition	Density (g/mL)	SPR
Soft	Water	H_2O	0.997	1.000
	Ethanol	C_2H_5OH	0.788	0.820
	n-Propanol	C_3H_7OH	0.803	0.840
	n-Butanol	C_4H_9OH	0.807	0.847
Bony	KP-1	K_2HPO_4(10.26%)	1.086	1.068
	KP-2	K_3HPO_4(20.81%)	1.189	1.146
	KP-3	K_2HPO_4(28.96%)	1.273	1.207
	KP-4	K_2HPO_4(34.64%)	1.336	1.253

Known properties of experimental inserts.

4. RESULTS

Experiments

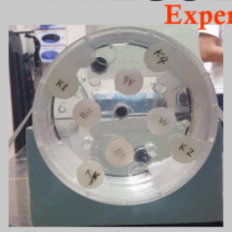

Fig 4.1 Experimental setup of helical scans

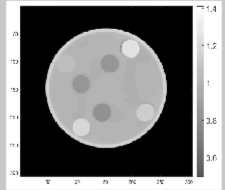

Fig 4.2 SPR image of helical experimental scans reconstructed using 3D helical JSIR-BVM.

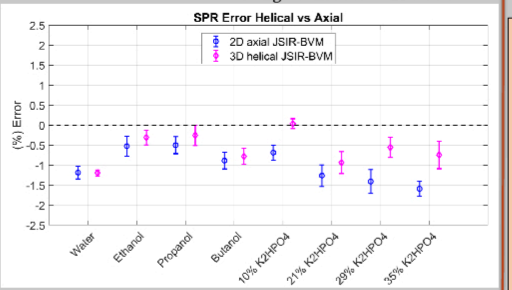

Fig 4.3 Percent error between reconstructed SPR values in an insert's 24 mm ROI and SPR values calculated from substances known densities and compositions[4].

Simulation

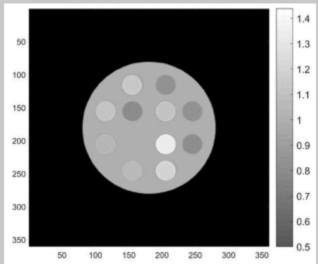

Fig 4.4 SPR image of simulated helical scans with 100% relative source intensity reconstructed using 3D JSIR-BVM.

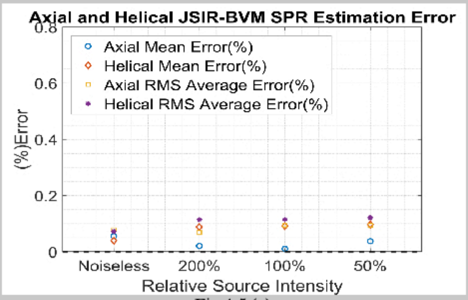

Fig 4.5 (a)

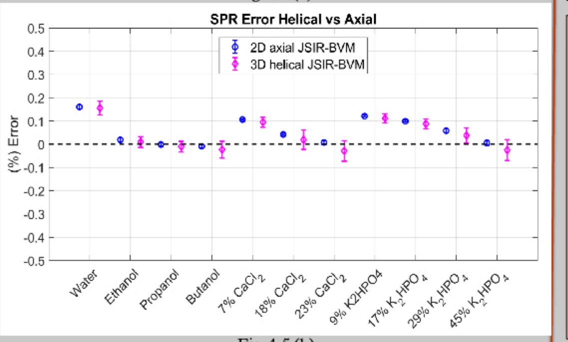

Fig 4.5 (b)

Fig 4.5 (a) Mean and RMS average error between reconstructed SPR and ground truth for 3D helical and 2D axial JSIR-BVM reconstructions of simulated scans for different noise levels. Mean errors are averaged over the insert 24 mm ROI pixels. RMS average error is the average of the insert RMS errors.
Fig 4.5 (b) Mean (data point) and standard deviation (bars) of percent error between reconstructed SPR values from noiseless simulated helical scans in an insert's 24 mm ROI and SPR values calculated using substance's known densities and compositions[4].

Elapsed Time

	Time per Iteration (s)	Time to Solution (hour)
Single-threaded CPU	3527	2797 (Predicted)
20-threaded CPU	760	602 (Predicted)
4 GPUs	29	18
GPU + Initial Guess + 33 Ordered Subsets	56	1.5
GPU + Initial Guess + 33 Ordered Subsets + Accelerated DEAM with spatially decoupled surrogate function[9]	48	0.4

3D JSIR-BVM is implemented on a computer equipped with Intel Xeon E5 2630-v4, 128 GB/2400MHz memory and 4 GeForce GTX 1080 Ti. Test measured data size: 10560 × 816 × 16. Test reconstructed image size: 610 × 610 × 42. Details on implemented Accelerated DEAM method can be found in Zhang[9].

Reconstruction of 3D Image Set from a Human Subject's DECT Scan

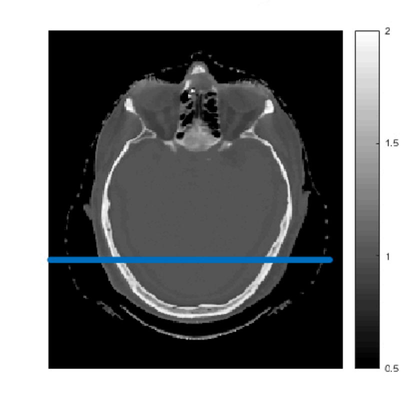

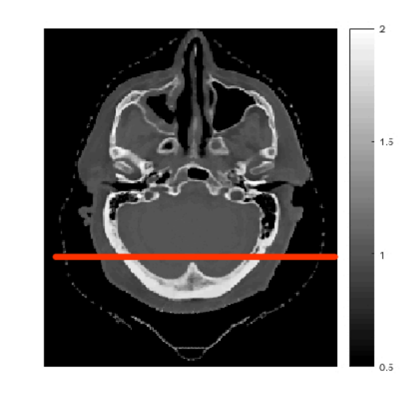

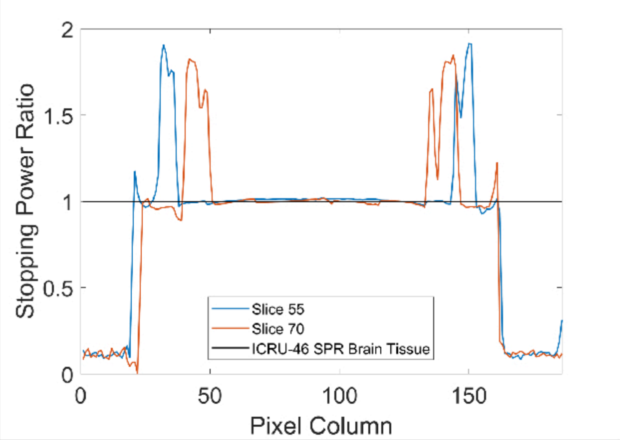

Fig 4.6 Slices 55 (Left) and 70 (center) from the reconstructed 3D SPR map of a brain tumor patient. (Right) Profiles through both slices SPR maps showing a mean SPR of 1.0 for cerebral tissue. Benchmark ICRU- value is 0.998.

5. CONCLUSIONS

- To our knowledge, **3D JSIR-BVM**[10] is the first SIR algorithm that directly reconstructs 3D SPR maps by simultaneously operating on experimentally-acquired, energy-uncompensated helical CT sinograms.
- We demonstrated its accuracy against experimental benchmarks, simulated ground truth, and SPR maps predicted by our 2D axial JSIR-BVM code.
- We were able to show early results of 3D SPR maps reconstructed from patient serial 90 and 140 kVp dual-energy, helical-CT scans acquired on a 16-slice Philips Big Bore Brilliance scanner.

Future work

- Studies must be performed to analyze inter- and intra-patient variabilities in SPR estimates and the susceptibility of our algorithm to errors in heterogeneous tissue with features smaller than an image voxel size.
- Further speed up our current method in order to do a full spiral reconstruction within a clinically acceptable time of 20 minutes.
- Mitigate effects of scatter in clinically realistic beam collimations. Unlike previous experiments in which axial scans could be acquired at the narrowest collimation, helical scans can only be obtained at 12 or 24 mm beam collimations which can be significantly affected by scatter.

6. ACKNOWLEDGMENTS

NIH National Institutes of Health supported by R01 CA 212638.

7. REFERENCES

1. H. Paganetti. Range uncertainties in proton therapy and the role of Monte Carlo simulations, Physics in Medicine & Biology 57 (2012) R99-R117.
2. B. C. Baumann, et al. Comparative effectiveness of proton therapy versus photon therapy as part of concurrent chemoradiotherapy for locally advanced cancer, Journal of Clinical Oncology, 2019.
3. S. Zhang, et al. Impact of joint statistical dual-energy CT reconstruction of proton stopping power images: Comparison to image- and sinogram-domain material decomposition approaches, Medical Physics 45 (2018) 2129–2142.
4. S. Zhang, et al. Experimental implementation of a joint statistical image reconstruction method for proton stopping power mapping from dual-energy CT data, Medical Physics 46 (2019) 273–285.
5. D. Han, et al. A linear, separable two-parameter model for dual energy CT imaging of proton stopping power computation. Medical Physics 2016;43:600–612.
6. D. Han, et al. On the accuracy of parametric two-parameter photon cross-section models in dual-energy CT applications. Medical Physics 2017;44:2438–2446.
7. J. A. O'Sullivan, et al. Alternating minimization algorithms for transmission tomography. IEEE Trans Med Imag. 2007;26:283–297.
8. S. Degirmenci, et al. Acceleration of iterative image reconstruction for x-ray imaging for security applications. Computational Imaging XIII. Vol. 9401. International Society for Optics and Photonics, 2015.
9. Zhang, Shuangyue, "Basis Vector Model Method for Proton Stopping Power Estimation using Dual-Energy Computed Tomography" (2018). Engineering and Applied Science Theses & Dissertations. 395.
10. A. Mitra, et al. Multi-GPU acceleration of branchless distance driven projection and backprojection for clinical helical CT. Electronic Imaging, Computational Imaging XV, pp. 36-48(13).

8. CONTACT INFORMATION

mariamedrano@wustl.edu

getao@wustl.edu